PHOTONICS Research

Dual-polarization programmable metasurface modulator for near-field information encoding and transmission

Lei Chen,[1] Qian Ma,[2] Qian Fan Nie,[1] Qiao Ru Hong,[2] Hao Yang Cui,[1] Ying Ruan,[1] and Tie Jun Cui[2,*]

[1]College of Electronics and Information Engineering, Shanghai University of Electric Power, Shanghai 200090, China
[2]State Key Laboratory of Millimeter Wave, Southeast University, Nanjing 210096, China
*Corresponding author: tjcui@seu.edu.cn

Received 12 October 2020; revised 6 December 2020; accepted 6 December 2020; posted 7 December 2020 (Doc. ID 412052); published 21 January 2021

Controlling the polarization state of electromagnetic waves is an important topic in microwaves due to the enormous application potential in radar technology and mobile communications. Here, we propose a programmable metasurface based on single-pole double-throw switches to realize multifunctional polarization conversions. A structure of the double-sided metallic pattern is adopted in the metasurface, in which a novel double-pole double-throw hub is achieved to guide the energy direction. Such a mechanism successfully induces multiple transmission channels into the metasurface structure for functional design. By controlling the states of the switches with a field programmable gate array, the *x*- and *y*-polarizations of the incident waves can be efficiently modulated into linear co- and cross-polarizations of transmitted waves, suggesting a higher degree of freedom on wave manipulations. The proposed metasurface can be developed as a near-field information encoder to transmit binary coding sequence according to the energy distribution. Character transmissions are realized by programming binary ASCII codes on the transmitted fields. Nine supercells on the metasurface can encode 9-bit binary information in one frame of near-field imaging, which can be switched in real time with high speed. We envision that this work will develop digital coding applications to control the polarization information.

https://doi.org/10.1364/PRJ.412052

1. INTRODUCTION

Metamaterials are artificially synthesized structures engineered to obtain effective permittivity and permeability that do not exist in nature. Compared to natural materials, metamaterials possess ground-breaking properties for electromagnetic (EM) [1–3], acoustic [4–6], and thermal [7–9] waves, which give rise to a rich variety of applications such as broadband absorbers [10], negative reflection [11], and thermal emitters [12]. As the two-dimensional (2D) version of metamaterials, metasurfaces have advantages in power consumption, weight, volume, and processing difficulty [13,14]. In addition, metasurfaces are able to tailor EM waves [15] dynamically by designing material structures elaborately. This distinctive property gives metasurfaces considerable potential applications in tuning EM waves, including absorption [16,17], wavefront manipulation [18,19], and polarization conversion [20]. Different from analog metasurfaces [21–24], described by effective medium parameters, it is now possible for digital metasurfaces to modulate EM waves by digital numbers [25–28]. By digitizing specific physical parameters, a bridge between the physical world and digital world has been built. Nevertheless, polarization regulation is rarely involved in digital coding metasurfaces.

Since polarization carries valuable information in signal transmission, it occupies a peculiar position among numerous characteristics of the EM waves. Manipulating polarization is extremely significant for practical applications ranging from communicating [29] to imaging [30]. To control the polarization of EM waves, various kinds of passive [31–33] and active [34–36] reconfigurable polarization converters have been proposed in recent literature. For passive converters, an asymmetric waveguide is adopted to realize polarization transformation. Another effective method uses a geometric phase in a metasurface structure to achieve spatially varying polarization conversion. In active polarization converters, PIN diodes are commonly introduced to accomplish conversion among different polarization states, including linear-to-linear [37] and linear-to-circular [38]. However, most of the aforementioned designs have a drawback in flexibility, for which they can only achieve one or two polarization conversion effects.

In this paper, we propose a programmable metasurface based on single-pole double-throw (SPDT) switches. Different from

the aforementioned works, this design employs switches based on silicon-on-insulator (SOI) technology, which offers high performance and ultralow cost. Two SPDT switches in a symmetrical structure form a double-pole double-throw (DPDT) switch to realize flexible selections on the incident and emitted waves. More importantly, since each SPDT switch can be controlled independently by a field programmable gate array (FPGA), the proposed metasurface is able to agilely encode binary polarization information on incident EM waves by a single programmable metasurface. We show that an ASCII code sequence of the characters contained in a 9-bit imaging frame of a near electric field can be completely transmitted. With low cost and easy fabrication, we believe our design extends the study of polarization and shows great potential applications in field information storage, processing, communications, and imaging.

2. RESULTS

To realize highly tunable polarization states, we propose a metasurface based on SPDT switches, as illustrated in Fig. 1. The metasurface enables the polarization of an incident wave to be tuned arbitrarily between the co- and cross-polarizations by changing the states of the SPDT switches. The states of switches are controlled via digital voltages supplied by the FPGA. Without losing the generality, here we design eight coding patterns using the proposed elements in various states to verify the polarization conversion. Under the illumination of linearly polarized waves, the metasurface can realize four linear-to-linear polarization transmission states: X-to-X, X-to-Y, Y-to-X, and Y-to-Y. Since each switch can be regulated separately, the metasurface can implement polarization manipulations in any desirable directions. When all switches are in the off states, the metasurface results in a perfect reflection. A symmetrical structure is employed on the front and back of the metasurface to establish two accesses for two orthogonal polarization conversions. Thus, the multifunctional metasurface with double-sided metallic patterns can realize the polarization modulations and reflections efficiently by switching the states of the SPDT switches.

A sketch of the adopted multilayer stacked element with a period $a = 40$ mm is exhibited in Fig. 2. The top three layers are symmetrical to the bottom three, which are spaced by prepreg layer (Arlon substrate, dielectric constant of 4.3 and loss tangent of 0.0035, marked with blue color) with a thickness $h_1 = 0.5$ mm. The top and bottom layers consist of a circular metal patch with a thickness 0.018 mm, a SPDT switch, and connecting lines. Since each SPDT switch can control two polarization states, every element possesses four states. For simplicity, we encode the x-polarized and y-polarized states as 0 and 1, respectively. Hence, the four states of the element are 00 (incident wave: x-polarized, emitted wave: x-polarized), 01 (incident wave: x-polarized, emitted wave: y-polarized), 10 (incident wave: y-polarized, emitted wave: x-polarized), and 11 (incident wave: y-polarized, emitted wave: y-polarized), which constitute 2-bit polarization digital states. A metal probe is used to connect the top and bottom structures. The two green layers are the same Arlon substrate with a thickness $h = 1$ mm and a metal ground with a thickness 0.018 mm, as illustrated in Fig. 2(a). As shown in Fig. 2(d), these ground planes pave the whole metasurface in the second and third layers, which are used as the reference ground when the top patch couples the energy from space and radiates in the bottom patch. Also, these ground planes can block the extra energy to transmit the metasurface. After numerous simulations and optimizations of the element with various structural sizes via CST Microwave

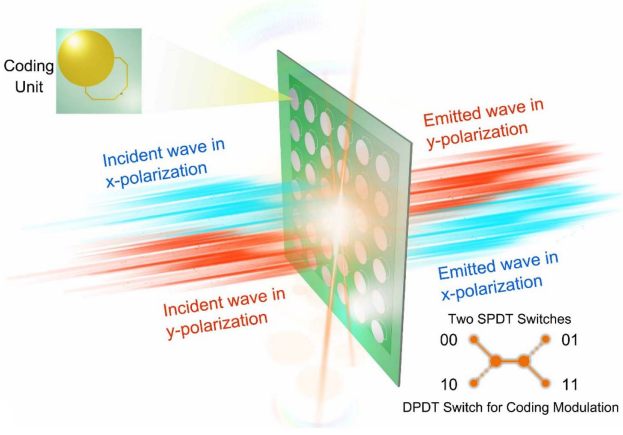

Fig. 1. Schematic of the proposed metasurface for polarization modulations in transmission mode. By controlling the states of the SPDT switches, the metasurface with double-sided metallic patterns can realize four linearly polarized states (X-to-X, X-to-Y, Y-to-X, and Y-to-Y) and perfect reflection.

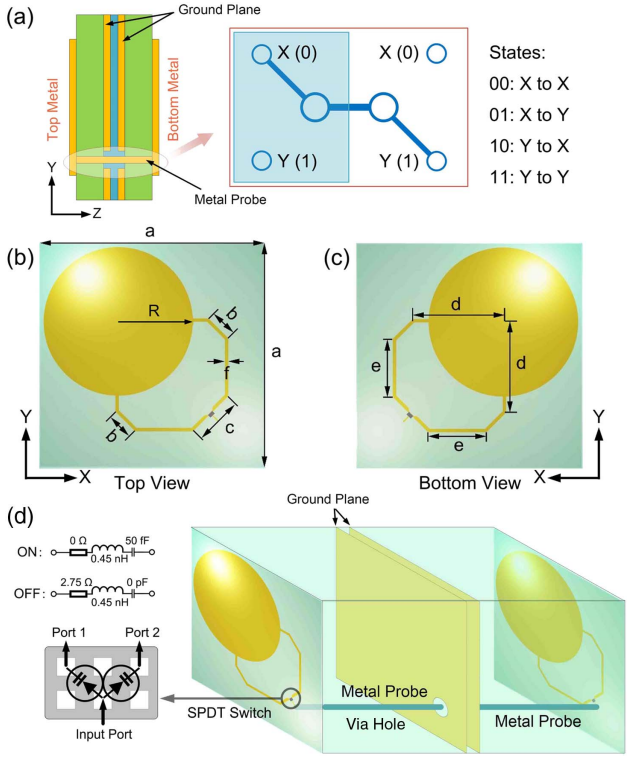

Fig. 2. Exposition of the multilayer element with specific parameters. (a) Profile of the adopted element and the states of the SPDT switches. (b) Top view and (c) bottom view of the element. (d) 3D view of the element structure.

Studio, we obtain the optimal geometrical parameters, as shown in Figs. 2(b) and 2(c). The more detailed dimensions of the element are designed as $R = 13.2$ mm, $b = 5$ mm, $c = 8.8$ mm, $d = 16.2$ mm, $e = 10.3$ mm, and $f = 0.6$ mm. In the design and optimization process, the main target is to achieve high transmission efficiency and good polarization selection, which is mainly related to the patch structure, material loss, and switch performance. By simulating and sweeping plentiful dimension combinations, we finally select a dimension combination with the best transmission efficiency. The optimization of the polarization selectivity follows a similar process. Figure 2(d) provides a 3D view of the element structure, in which the thickness between the top and bottom layers is visually increased to clearly exhibit the inner structure. The spatial energy coupled by the top circular patch is guided through the specific channel to transmit under the control of two SPDT switches. The SPDT switch is a rectangular chip with six pins. The pin configuration and its equivalent circuit of the SPDT switch are also provided in Fig. 2(d), where the input pin is connected with two transistors as the RF switches. We use a series RLC circuit model in simulations to represent the on and off states, as shown in Fig. 2(d).

To further understand the polarization conversion behavior and verify the design, numerical simulations of the element are carried out using CST Microwave Studio. In the simulations, periodic boundaries are set, and the SPDT switch is modeled as an RLC series circuit in the on/off state. In the on state, $R = 2.75\ \Omega$, $L = 0.45$ nH, and $C = 0$ pF; in the off state, $R = 0\ \Omega$, $L = 0.45$ nH, and $C = 0.05$ pF. Figure 3 shows the transmission characteristics of co-polarized and cross-polarized waves for the element in different states. Considering a transmission system composed of two antennas and a metasurface, the energy component is transmitted or converted into the specific polarization. By applying the properties of DPDT in Fig. 2(b), four distinct states are achieved, as marked in different colors in Fig. 3(a). For instance, when the element is illuminated normally by the x-polarized wave, the unit cell in state 00 can realize the co-polarization. For state 01, the incident x-polarized wave is converted to the y-polarized wave. At 2.77 GHz, the transmission coefficient of the co-polarized wave

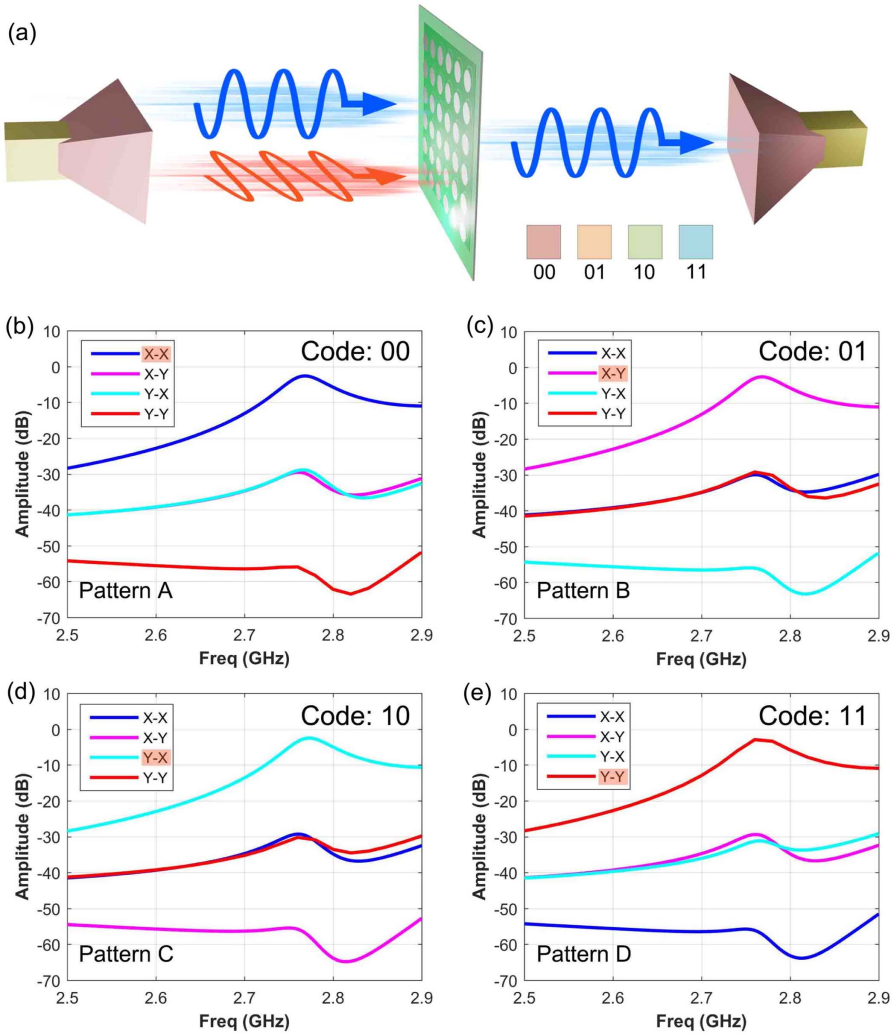

Fig. 3. (a) Designed modulation situation and digital coding patterns. (b)–(e) Simulated amplitudes of the transmission coefficients for elements in the states of (b) 00, (c) 01, (d) 10, and (e) 11, corresponding to patterns A, B, C, and D.

is approximately −3.66 dB for state 00, and that of the cross-polarized wave is around −3.65 dB for state 01, as depicted in Figs. 3(b) and 3(c). Please note that the transmission loss mainly comes from the lossy resistor in the circuit model of SPDT, which can be resolved using low-loss chips. Under the *y*-polarized incidence, the cross-polarization transmission of state 10 reaches about −3.65 dB, as shown in Fig. 3(d), which means that most of incident wave is converted to its orthogonal polarization at 2.77 GHz. Likewise, in Fig. 3(e), when the unit cell works in state 11, only the *y*-polarized wave can pass through the metasurface. For these four states, the difference between the transmitted and the nontransmitted amplitudes is about 25 dB at the central frequency. Thus, with good isolation between the different states, the polarization of the transmitted wave can be distinctly modulated by different states of the DPDT switches, making a tunable and programmable polarization converter.

By encoding the four metasurface elements (00, 01, 10, and 11), we design eight distinct coding patterns to demonstrate the diverse programmable ability of the transmitted wave. The whole metasurface consists of 6 × 6 elements integrated with 72 SPDT switches, and the overall size is 240 mm × 240 mm. First, we arrange the uniform patterns (all elements in the same state), respectively, using the states 00, 01, 10, and 11, as four patterns (A, B, C, and D), whose transmission characteristics are illustrated in Fig. 3. The combination of the four coding states will enable more flexible transmission manipulations for different polarizations. Considering the symmetrical and reciprocal features, we present another four representative patterns (E, F, G, and H) with distinctly mixed coding patterns, as depicted in Figs. 4(a)–4(d), in which the coding sequences are expressed as 00010001, 10111011, 00110011, and 00010001/10111011. To clearly exhibit their functions, the transmitted powers between the *x*- and *y*-polarizations are

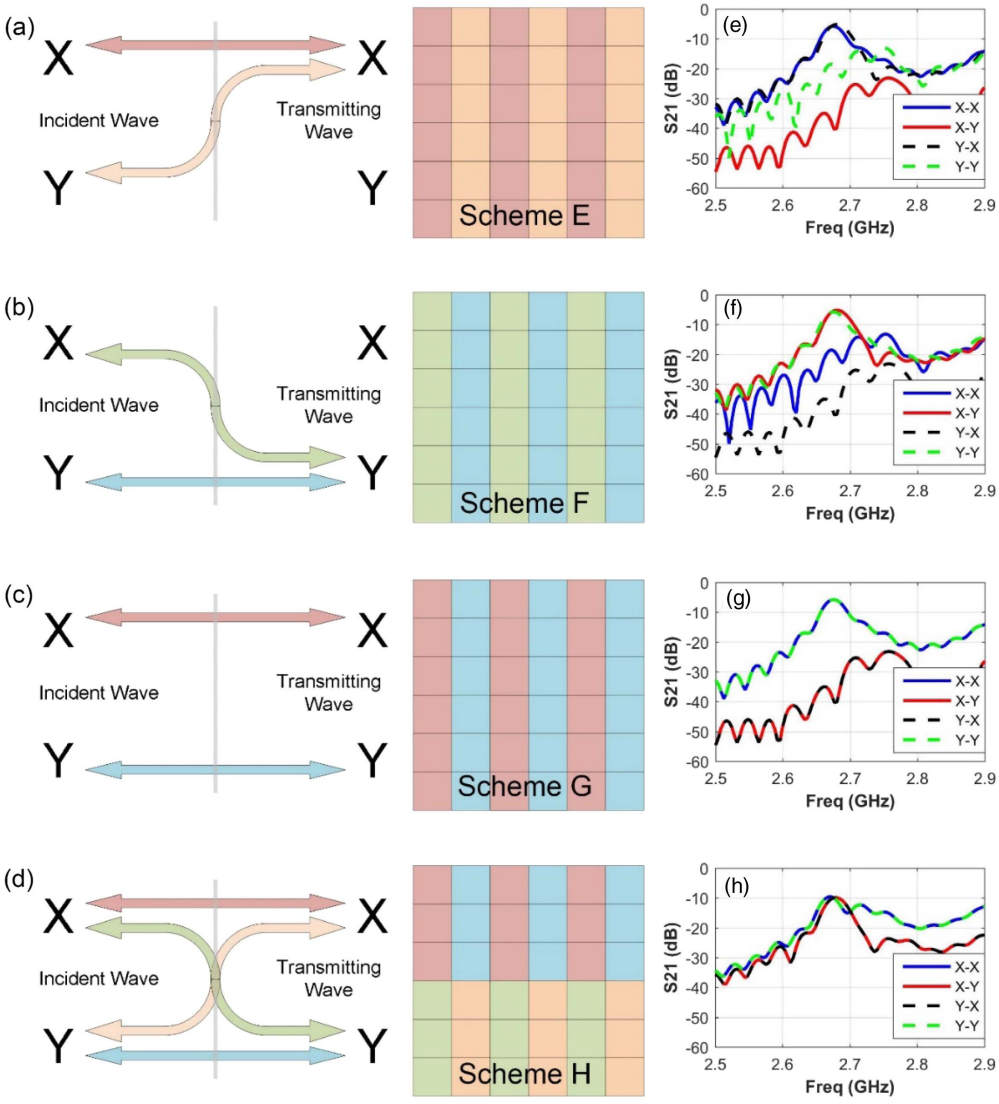

Fig. 4. Combined coding patterns and related simulation results. (a)–(d) Representative combined coding patterns (E, F, G, and H) with multifunctionalities expressed as 00010001, 10111011, 00110011, and 00010001/10111011, as well as the transmission power illustrations. (e)–(h) Related simulation results of transmission coefficients, in which the data of all four channels are included (X–X, X–Y, Y–X, and Y–Y).

indicated with arrow-shaped components, in which the bidirectional arrow shape suggests the reciprocity of transmissions and conversions. In addition, the colors of the arrow components are related to the codes illustrated in Fig. 4.

We clearly see that each kind of coding element enables a channel of metasurface for the transmitted wave, such as the *x*- and *y*-polarized transmissions or polarization conversions. Once two or more kinds of coding elements are programmed, the relevant channels are activated, as shown in Figs. 4(a)–4(d). The related simulation results are provided in Figs. 4(e)–4(h), in which the transmission states of four channels are clearly observed, showing good consistency with the element performance. The simulation configuration is the same as that illustrated in Fig. 3(a), in which the two horn antennas are placed 500 mm away from the metasurface. In patterns E, F, and G, two kinds of coding elements with the same amount are grouped in the patterns, and the related results are presented, respectively, in Figs. 4(e)–4(g), in which the maximum transmission coefficient (S21) is about −6 dB at 2.68 GHz. The other channels in these patterns are closed. Hence, the magnitudes of S21 in these channels are much lower than in the single transmitting channels. In pattern H, all four channels are enabled, and the maximum transmission coefficient S21 further reduces by about 3 dB compared to patterns E–G, because only a quarter of the elements are programmed for one channel. It should be noted that in the simulation of each channel, the polarizations of the transmitting and receiving horn antennas are set for the related polarization of the channel. We should also notice that in patterns A, B, and D, we intend to present the spatial energy conversion between two orthogonal

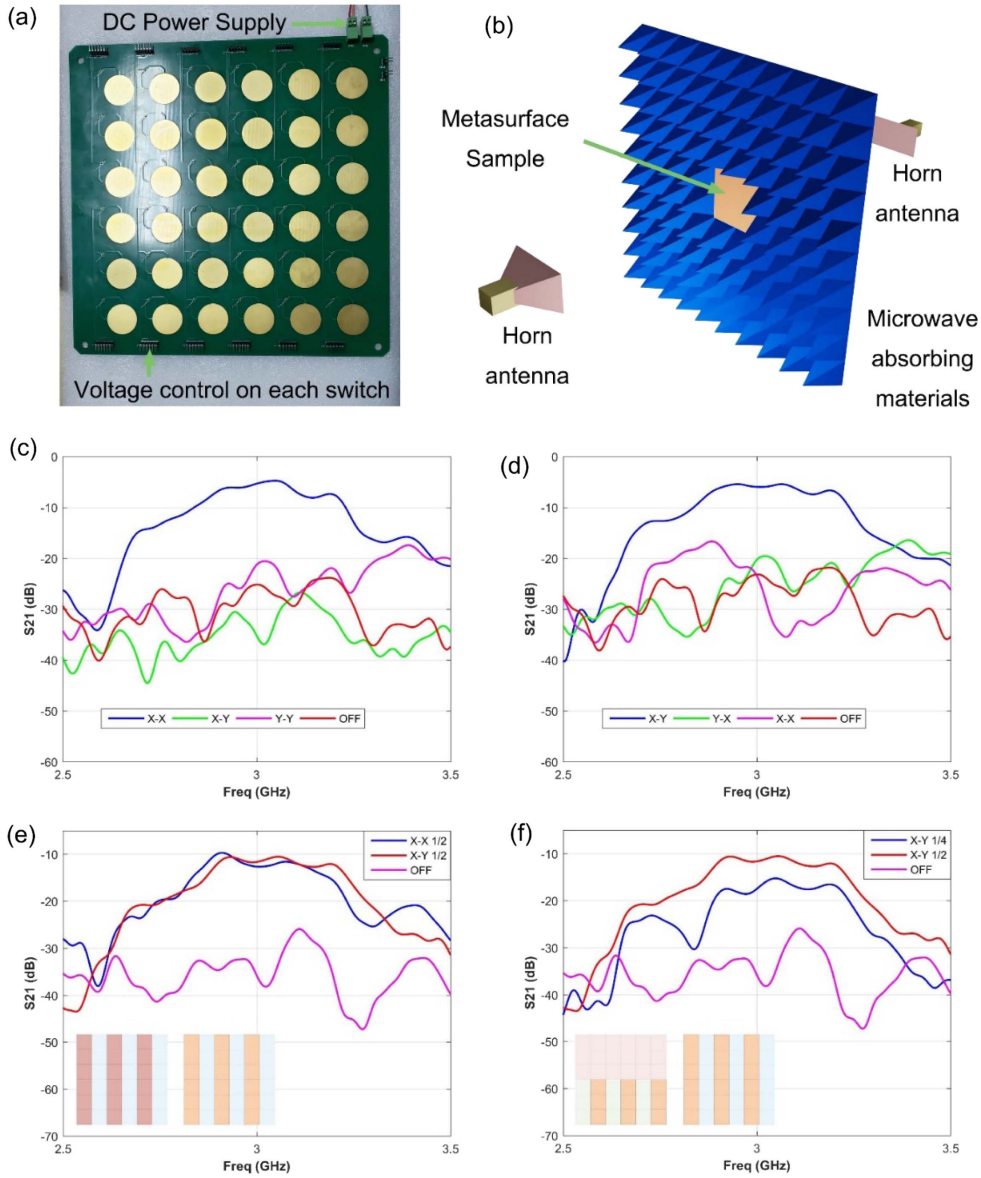

Fig. 5. Experimental setup of the proposed programmable metasurface. (a) Photograph of the fabricated sample. (b) Schematic of the experimental setup. (c)–(f) Measured transmission coefficients S21 of: (c) pattern A; (d) pattern B; (e) pattern E; and (f) pattern F.

polarizations, which cannot be used for information transmissions. On the contrary, in pattern C, two independent channels are established for low-interference transmissions.

To confirm the validity of the simulations, a prototype was fabricated using printed circuit board (PCB) technology. The overall metasurface and an enlarged element are exhibited in Fig. 5(a). The switch chip is fabricated using SOI technology and is soldered on the metasurface. The DC power supply is 2.5 V, which ensures that the DPDT switch works properly. Since each switch needs a digital control voltage to change the on and off states, the designed metasurface has 72 voltage control electrodes connecting to the FPGA. As a result, the state of each element can be selected flexibly. The experimental characterization of the programmable metasurface is performed in a microwave anechoic chamber by using a vector network analyzer with two horn antennas as the EM wave source and receiver, as shown in Fig. 5(b). To diminish the effect caused by the reflected waves in experiments, the metasurface sample is fixed using microwave absorbing material. The incident EM wave is linearly polarized and the S-parameters are measured by the receiving antenna for cross-polarized and co-polarized transmitted waves.

Due to the symmetrical property, the X–X or X–Y polarization transmission can be easily induced by rotating the whole system 90 deg. Therefore, we select four representative patterns for measurements. Due to the slight frequency offset in the measurement results, we extend the frequency range from 2.5 to 3.5 GHz in the data plot. In Figs. 5(c) and 5(d), it can be clearly observed that the gains of the co-polarized transmitted waves (X–X) for pattern A and cross-polarized waves (X–Y) for pattern B are about −5.5 dB at 3 GHz, when the metasurface is excited by the *x*-polarized EM waves. Meanwhile, the other two channels Y–Y and Y–X have good isolations, which remain at about −20 dB. The transmission loss mainly results from the loss resistor of the SPDT switch and the structure loss. In addition, the combined patterns E and H are measured and presented in Figs. 5(e) and 5(f), where the activated elements are marked in specific colors. As depicted in Fig. 5(e), the blue curve represents the result of pattern E, in which only the elements 00 (in red) are activated, while the red

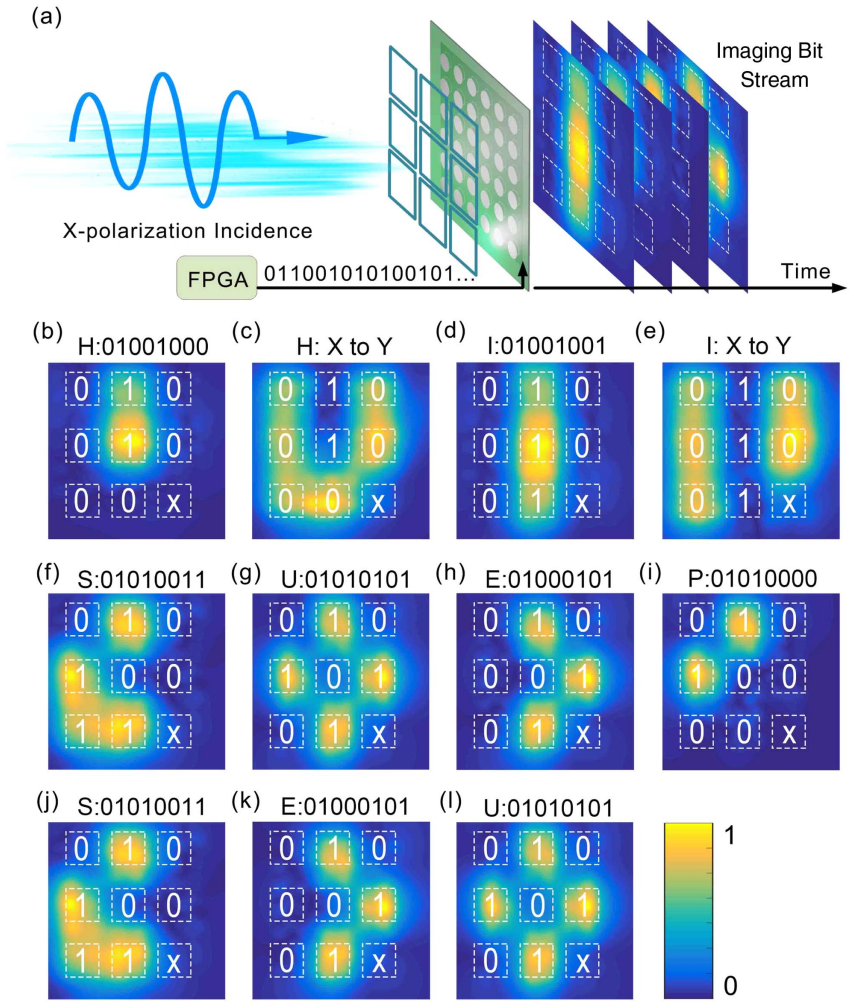

Fig. 6. Design and simulations of near-field information transmission using binary ASCII codes. (a) Schematic of the binary information representation and transmission. (b)–(l) Simulated near-field electric field distributions of three groups of letters in binary ASCII codes: HI, SUEP, and SEU.

curve indicates the transmission coefficient (S21) of the metasurface with only half elements 01 (in orange) being activated. Comparing Figs. 5(c) and 5(d), the transmission coefficients of the metasurface in these two cases are slightly lower by about 3 dB. This is because only half of the elements of the metasurface are activated for one channel (X–X), while the other half are activated for the other channel (X–Y). Likewise, in Fig. 5(f), the measured power (in blue) of pattern F for only a quarter of the activated elements 01 is lower than the case when half of the elements 01 are excited. Compared to the simulated results, the power levels of the measured patterns have good agreement, and the slight frequency deviation is due to the error in PCB fabrication and circuit modeling. Besides, when the SPDT switches in each element are in the off states, the transmission coefficients S21 of the four coding patterns are all below −20 dB, indicating that the metasurface can achieve prefect reflections.

The metasurface is composed of 6 × 6 elements, which can be divided into nine supercells. Here, a supercell consists of 2 × 2 elements that share the same transmission state, as shown in Fig. 6(a). The state is directly controlled by the biased voltage from FPGA. Under the influence of a specific linear polarization incidence, the transmitted wave can be characterized with different amplitude distributions in the near field of the metasurface. The nine supercells possess different transmission energies, and hence we can encode the supercell with a high or low transmission energy as digit 1 or 0, whose information bit can be easily identified according to its energy level. To verify the above-mentioned information transmission performance, we design a simulation to transmit ASCII codes of letters. Since the metasurface is comprised of nine supercells, we regard them as nine bits according to the corresponding transmission positions of the supercells. The first eight supercells use 8-bit binary ASCII codes of letters, and the ninth supercell is viewed as 0 flag bit (using code 01 for isolation). To briefly represent the binary coding information, we arrange an *x*-polarized incidence and codes 11 and 10 (previously illustrated in Figs. 3 and 4) in the near-field information transmission as binary 1 and 0.

Take the letter H as an example, whose binary ASCII code is 01001000. Under the control of the FPGA, the state of the second and fourth supercells is set as X-to-X polarization (encoded as 1), and the state of the remaining six supercells is set as X-to-Y polarization (encoded as 0). In Fig. 1(b), when the *x*-polarized wave is incident, we observe that the energy of the *x*-polarized transmitted wave is mainly concentrated on the second and fourth supercells, whose corresponding information code is 01001000, indicating the letter H. Thus, the information can be transmitted through the energy levels of the supercells. Under the same setting, the energy distribution of the *y*-polarized transmitted wave is just opposite to the *x*-polarized, as shown in Fig. 6(c). In the same way, we can characterize other letters by setting specific supercell states. Figures 6(d) and 6(e) represent the letter I (the two graphs have opposite energy distributions for the same reason). As shown in

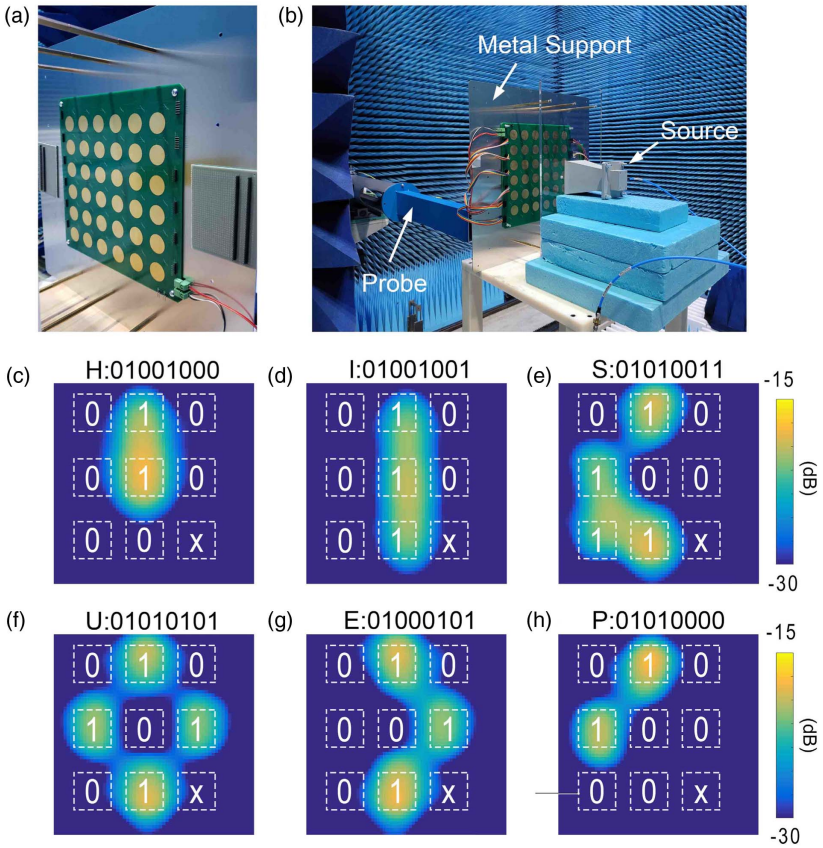

Fig. 7. Experimental demonstrations of the near-field information transmissions using binary ASCII codes. (a), (b) Configuration of near-field measurements. (c)–(h) Measured results of six letters represented with binary ASCII codes: (c) H, (d) I, (e) S, (f) U, (g) E, and (h) P.

Figs. 6(d) and 6(e), the energy graphs of both metasurfaces represent the letter I. Consequently, we can recognize the letters represented by Figs. 6(f)–6(l) as S(01010011), U(01010101), E(01000101), P(01010000), and S, E, U, respectively. We remark that the horizontal dimension of the near-field result is slightly compressed; hence, the white boxes indicating 0 and 1 are not uniformly spaced. The slightly inhomogeneous energy distribution and position deviation are mainly due to two reasons: 1) a nonideal wavefront is generated from the horn antenna; and 2) cross coupling exists between adjacent elements.

We perform near-field measurements to demonstrate the encoded information transmission. As presented in Figs. 7(a) and 7(b), the metasurface is fixed on a metal supporting plate, joined to an acrylic board using six copper cylinders. The metal plate around the metasurface also prevents the additional diffraction energy from interfering with the transmitted near field. A broadband horn antenna is placed in front of the metasurface as the feeding source. An S band waveguide probe is arranged at the distance of 20 mm away from the metasurface to test the 2D electric field distribution. The feeding horn and probe are both along the x axis. The element employs the code 10 as digit 0 and code 11 as digit 1, which, respectively, execute the X–to–Y and X–to–X polarization conversion and transmission. Six ASCII code sequences of six letters H, I, S, U, E, and P are measured, as shown in Figs. 7(c)–7(h), where digits 0 and 1 represent the transmitted signal energy levels. Obviously, the measured results of these ASCII sequences are clearly distinguished, showing good agreement with the simulation results in Fig. 6. Compared to the simulations, the measured results seem more uniform than the simulated ones, which mainly result from different colorbar ranges and scales. Based on the energy diagrams of transmitted waves, we can conclude that the imaging-bit information of letters H, I, S, U, E, and P has been successfully transmitted. Since the polarization selectivity has already been demonstrated in Fig. 5 and we mainly intend to demonstrate the information representation and transmission using the presented metasurface, we believe that the measurements in the x-polarization have fully validated our scheme.

3. CONCLUSION

We demonstrated a novel programmable metasurface integrated with the SPDT switches on the top and bottom metallic layers. By controlling the SPDT switches in each element, we can convert the transmitted EM waves between the linear cross- and co-polarizations. Each element has four polarization states encoded as 00, 01, 10, and 11. We have programmed different element states into various sequences to further manipulate the polarizations of the transmitted EM waves. Besides the switchable polarization conversions, a perfect reflection is achieved when all switches on the metasurface work in the off state. It should be noted that the presented metasurface only supports plane waves at normal incidence. For oblique incidence, the structure and period dimension must be redesigned for higher diffraction orders. More importantly, we can further modulate the information on near-field distributions using the single programmable metasurface. Six characters in binary ASCII code sequences are designed, simulated, and measured. Both simulated and measured results proved good performance and high flexibility, indicating that the proposed design has a great effect on polarization conversions and dynamic field information editing and transmission. We envision that this work will enrich the programmable dimension of information metasurfaces [39,40] and facilitate the next generation of wireless communications and imaging.

Funding. National Natural Science Foundation of China (11404207, 61571117, 61631007); SHIEP Foundation (K2014-054, Z2015-086); Local Colleges and Universities Capacity Building Program of the Shanghai Science and Technology Committee (15110500900); National Key Research and Development Program of China (2017YFA0700201, 2017YFA0700202, 2017YFA0700203); Fund for International Cooperation and Exchange of National Natural Science Foundation of China (61761136007).

Disclosures. The authors declare no conflicts of interest.

REFERENCES

1. T. J. Cui, M. Q. Qi, X. Wan, J. Zhao, and Q. Cheng, "Coding metamaterials, digital metamaterials and programmable metamaterials," Light Sci. Appl. **3**, e218 (2014).
2. A. V. Kildishev, A. Boltasseva, and V. M. Shalaev, "Planar photonics with metasurfaces," Science **339**, 1232009 (2013).
3. H. T. Chen, A. J. Taylor, and N. Yu, "A review of metasurfaces: physics and applications," Rep. Prog. Phys. **79**, 076401 (2016).
4. L. Wu, M. Oudich, W. Cao, H. Jiang, and Y. Jing, "Routing acoustic waves via a metamaterial with extreme anisotropy," Phys. Rev. Appl. **12**, 044011 (2019).
5. G. Hu, L. Tang, and X. Cui, "On the modelling of membrane-coupled Helmholtz resonator and its application in acoustic metamaterial system," Mech. Syst. Sig. Process. **132**, 595–608 (2019).
6. N. G. R. de Melo Filho, C. Claeys, E. Deckers, and W. Desmet, "Realisation of a thermoformed vibro-acoustic metamaterial for increased STL in acoustic resonance driven environments," Appl. Acoust. **156**, 78–82 (2019).
7. B. L. Davis and M. I. Hussein, "Nanophononic metamaterial: thermal conductivity reduction by local resonance," Phys. Rev. Lett. **112**, 055505 (2014).
8. Y. Guo and Z. Jacob, "Thermal hyperbolic metamaterials," Opt. Express **21**, 15014–15019 (2013).
9. T. Han, X. Bai, J. T. Thong, B. Li, and C. W. Qiu, "Full control and manipulation of heat signatures: cloaking, camouflage and thermal metamaterials," Adv. Mater. **26**, 1731–1734 (2014).
10. M. Li, S. Q. Xiao, Y. Y. Bai, and B. Z. Wang, "An ultrathin and broadband radar absorber using resistive FSS," IEEE Antennas Wireless Propag. Lett. **11**, 748–751 (2012).
11. S. Zuo, Y. Cheng, and X. Liu, "Tunable perfect negative reflection based on an acoustic coding metasurface," Appl. Phys. Lett. **114**, 203505 (2019).
12. X. Liu, T. Tyler, T. Starr, A. F. Starr, N. M. Jokerst, and W. J. Padilla, "Taming the blackbody with infrared metamaterials as selective thermal emitters," Phys. Rev. Lett. **107**, 045901 (2011).
13. N. Yu, P. Genevet, M. A. Kats, F. Aieta, J. P. Tetienne, and F. Capasso, "Light propagation with phase discontinuities: generalized laws of reflection and refraction," Science **334**, 333–337 (2011).
14. Q. Ma, C. B. Shi, G. D. Bai, T. Y. Chen, A. Noor, and T. J. Cui, "Beam-editing coding metasurfaces based on polarization bit and orbital-angular-momentum-mode bit," Adv. Opt. Mater. **5**, 1700548 (2017).
15. L. Zhang, R. Y. Wu, G. D. Bai, H. T. Wu, Q. Ma, and X. Q. Chen, "Transmission-reflection-integrated multifunctional coding metasurface for full-space controls of electromagnetic waves," Adv. Funct. Mater. **28**, 1802205 (2018).

16. L. Chen, H. L. Ma, X. J. Song, Y. Ruan, and H. Y. Cui, "Dual-functional tunable coding metasurface based on saline water substrate," Sci. Rep. **8**, 2070 (2018).
17. S.-H. Li, J.-S. Li, and J.-Z. Sun, "Terahertz wave front manipulation based on Pancharatnam-Berry coding metasurface," Opt. Mater. Express **9**, 1118–1127 (2019).
18. Q. Ma, G. D. Bai, H. B. Jing, C. Yang, L. Li, and T. J. Cui, "Smart metasurface with self-adaptively reprogrammable functions," Light Sci. Appl. **8**, 98 (2019).
19. L. Chen, Q. Ma, H. B. Jing, H. Y. Cui, Y. Liu, and T. J. Cui, "Space-energy digital-coding metasurface based on an active amplifier," Phys. Rev. Appl. **11**, 054051 (2019).
20. P. C. Wu, W. Zhu, Z. X. Shen, and D. P. Tsai, "Broadband wide-angle multifunctional polarization converter via liquid-metal-based metasurface," Adv. Opt. Mater. **5**, 1600938 (2017).
21. H.-X. Xu, S. Tang, S. Ma, W. Luo, T. Cai, S. Sun, Q. He, and L. Zhou, "Tunable microwave metasurfaces for high-performance operations: dispersion compensation and dynamical switch," Sci. Rep. **6**, 38255 (2016).
22. C. Huang, C. Zhang, J. Yang, B. Sun, B. Zhao, and X. Luo, "Reconfigurable metasurface for multifunctional control of electromagnetic waves," Adv. Opt. Mater. **5**, 1700485 (2017).
23. Y. Zárate, I. V. Shadrivov, and D. A. Powell, "Tunable focusing by a flexible metasurface," Photon. Nanostr. Fundam. Appl. **26**, 62–68 (2017).
24. F. Callewaert, V. Velev, S. Jiang, A. V. Sahakian, P. Kumar, and K. Aydin, "Inverse-designed stretchable metalens with tunable focal distance," Appl. Phys. Lett. **112**, 091102 (2018).
25. Q. Ma, Q. R. Hong, G. D. Bai, H. B. Jing, and T. J. Cui, "Editing arbitrarily linear polarizations using programmable metasurface," Phys. Rev. Appl. **13**, 021003 (2020).
26. Z. Luo, M. Z. Chen, Z. X. Wang, L. Zhou, and T. J. Cui, "Digital nonlinear metasurface with customizable nonreciprocity," Adv. Funct. Mater. **29**, 1906635 (2019).
27. Q. Ma, Q. R. Hong, X. X. Gao, H. B. Jing, C. Liu, and G. D. Bai, "Smart sensing metasurface with self-defined functions in dual polarizations," Nanophotonics **9**, 3271–3278 (2020).
28. Q. Ma, L. Chen, H. B. Jing, Q. R. Hong, H. Y. Cui, and Y. Liu, "Controllable and programmable nonreciprocity based on detachable digital coding metasurface," Adv. Opt. Mater. **7**, 1901285 (2019).
29. M. R. Andrews, P. P. Mitra, and R. deCarvalho, "Tripling the capacity of wireless communications using electromagnetic polarization," Nature **409**, 316–318 (2001).
30. C. D. Stoik, M. J. Bohn, and J. L. Blackshire, "Nondestructive evaluation of aircraft composites using transmissive terahertz time domain spectroscopy," Opt. Express **16**, 17039–17051 (2008).
31. Y. Liu, Y. Hao, K. Li, and S. Gong, "Radar cross section reduction of a microstrip antenna based on polarization conversion metamaterial," IEEE Antennas Wireless Propag. Lett. **15**, 80–83 (2016).
32. X. Yu, X. Gao, W. Qiao, L. Wen, and W. Yang, "Broadband tunable polarization converter realized by graphene-based metamaterial," IEEE Photonics Technol. Lett. **28**, 2399–2402 (2016).
33. M. F. O. Hameed, S. S. A. Obayya, and H. A. El-Mikati, "Passive polarization converters based on photonic crystal fiber with L-shaped core region," J. Lightwave Technol. **30**, 283–289 (2012).
34. X. Ma, W. Pan, C. Huang, M. Pu, Y. Wang, and B. Zhao, "An active metamaterial for polarization manipulating," Adv. Opt. Mater. **2**, 945–949 (2014).
35. W. Li, S. Xia, B. He, J. Chen, H. Shi, and A. Zhang, "A reconfigurable polarization converter using active metasurface and its application in horn antenna," IEEE Trans. Antennas Propag. **64**, 5281–5290 (2016).
36. Z. Tao, X. Wan, B. C. Pan, and T. J. Cui, "Reconfigurable conversions of reflection, transmission, and polarization states using active metasurface," Appl. Phys. Lett. **110**, 121901 (2017).
37. Y. Cheng, W. Li, and X. Mao, "Triple-band polarization angle independent 90 degrees polarization rotator based on Fermat's spiral structure planar chiral metamaterial," Prog. Electromagn. Res. **165**, 35–45 (2019).
38. J. Zhao, X. Yang, J. Y. Dai, Q. Cheng, X. Li, and T. J. Cui, "Programmable time-domain digital-coding metasurface for non-linear harmonic manipulation and new wireless communication systems," Natl. Sci. Rev. **6**, 231–238 (2019).
39. Q. Ma and T. J. Cui, "Information metamaterials: bridging the physical world and digital world," PhotoniX **1**, 1 (2020).
40. T. J. Cui, L. Li, S. Liu, Q. Ma, and Q. Cheng, "Information metamaterial systems," iScience **23**, 101403 (2020).